

BGS candidate models for IGRF-14

Team institution: British Geological Survey
Team members: William Brown (wb@bgs.ac.uk)
Natalia Gomez-Perez
Callum Watson
Ciarán Beggan

Candidate models submitted: 1. DGRF main field at 2020.0
2. IGRF secular variation for 2025.0—2030.0
3. IGRF main field at 2025.0

1. Data sources and selection

Three data sources were used to construct our candidate models: (1) the ESA Swarm mission, (2) the Macau Science Satellite mission, and (3) the ground observatory network.

1.1 Ground observatories

Definitive hourly mean vector data were collected from the World Data Centre for Geomagnetism, Edinburgh for the period 2018/01/01 to 2023/12/31. These were supplemented with other more recent quasi-definitive and near-definitive data reported to INTERMAGNET, Tromsø Geophysical Observatory or from BGS, for the period up to 2024/09/23.

1.2 Swarm

The latest available 1 Hz Swarm data files, up to version 0606, were collected for Alpha, Bravo and Charlie, for the period 2018/01/01 to 2024/09/20.

1.3 MSS

The latest available 1 Hz MSS-1a data files, up to version 0431, were collected for the period 2023/11/02 to 2024/07/31.

1.4 Data selection criteria

The following selection criteria were applied to Swarm, MSS and observatory data, as summarised Table 1.

Satellite data were subsampled (every 20th datum) and were retained only for magnetically quiet times. At low geomagnetic dipole (GMD) latitudes only local nighttime data were retained, while at high GMD latitudes no local time selection was applied and filters for zenith angle and merging electric field were applied. We use vector data at all latitudes and only use a small number of scalar data, projected along a prior model vector, where there are no corresponding vector data available. Solar wind parameters were provided by the OMNI2 data set, which includes a forward projection of measurements made at the L1 Lagrange point to Earth's magnetopause.

We also use full field observatory data from 132 locations, at hourly mean cadence, and selected for local night times at all latitudes. Vector data from 94 observatories were used below GMD latitude $|\pm 55^\circ|$, and scalar data, projected along a prior model vector, from 38 observatories at higher latitudes.

Table 1: Summary of data selection criteria for Swarm, MSS and ground observatory data.

Filter	Description	Satellite	Observatory
Sampling	–	Every 20 th 1 Hz datum	Hourly mean
Kp, Kp _{-3h}	3-hour planetary K index at datum and in preceding 3 hour interval	$\leq 2_0, \leq 2_0$	$\leq 2_+$
D _{st} [nT], dD _{st} /dt [nT/h]	Storm time disturbance index and its rate of change per hour at datum	$\leq 30, \leq 2$	–, ≤ 5
IMF B _x , B _y , B _z [nT]	Projected Interplanetary Magnetic Field at datum	$\leq 10 , \leq 3 , 0 \leq x \leq 6$	–, –, ≥ -2
v _{sw} [km/s]	Projected solar wind velocity at datum	≤ 450	–
LT (< 55°GMD)	Local time at GMD latitudes below 55°	23:00 ≤ x ≤ 05:00	01:00 ≤ x ≤ 02:00
d-m _{prior} [nT]	Absolute difference between datum and a prior BGS field model estimation	≤ 100	–
F- B [nT]	Absolute difference between ASM and magnitude of VFM data	≤ 2	–
E _{min} (> 55°GMD) [mV/m]	Hourly mean of 1 minute merging electric field, calculated as in Olsen <i>et al.</i> [2014].	≤ 0.8	–
z (°)	Zenith angle at 110km altitude for datum at GMD latitudes above 55°	≥ 100.5	–

The resulting temporo-spatial distribution of data is shown in Figure 1. The separation of observatories between those providing vector data and those providing projected-scalar data is shown in Figure 2. A total of 5,162,040 data were used.

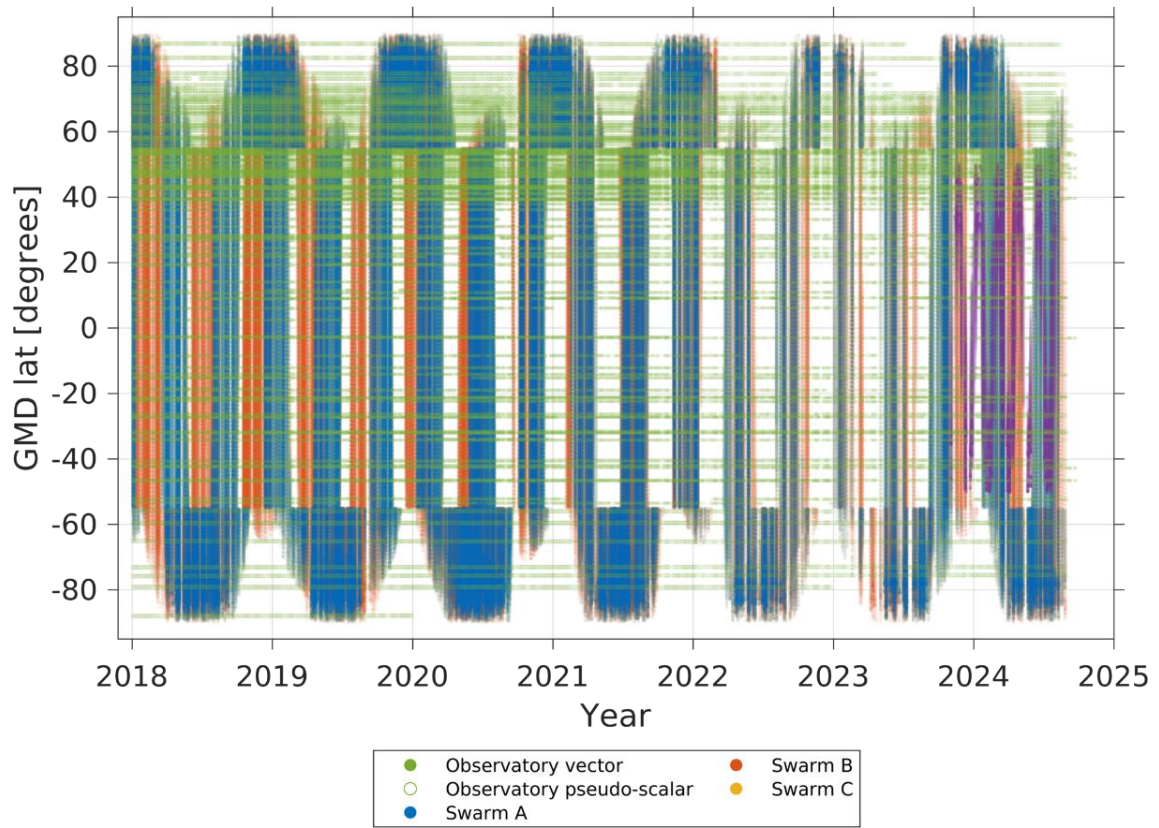
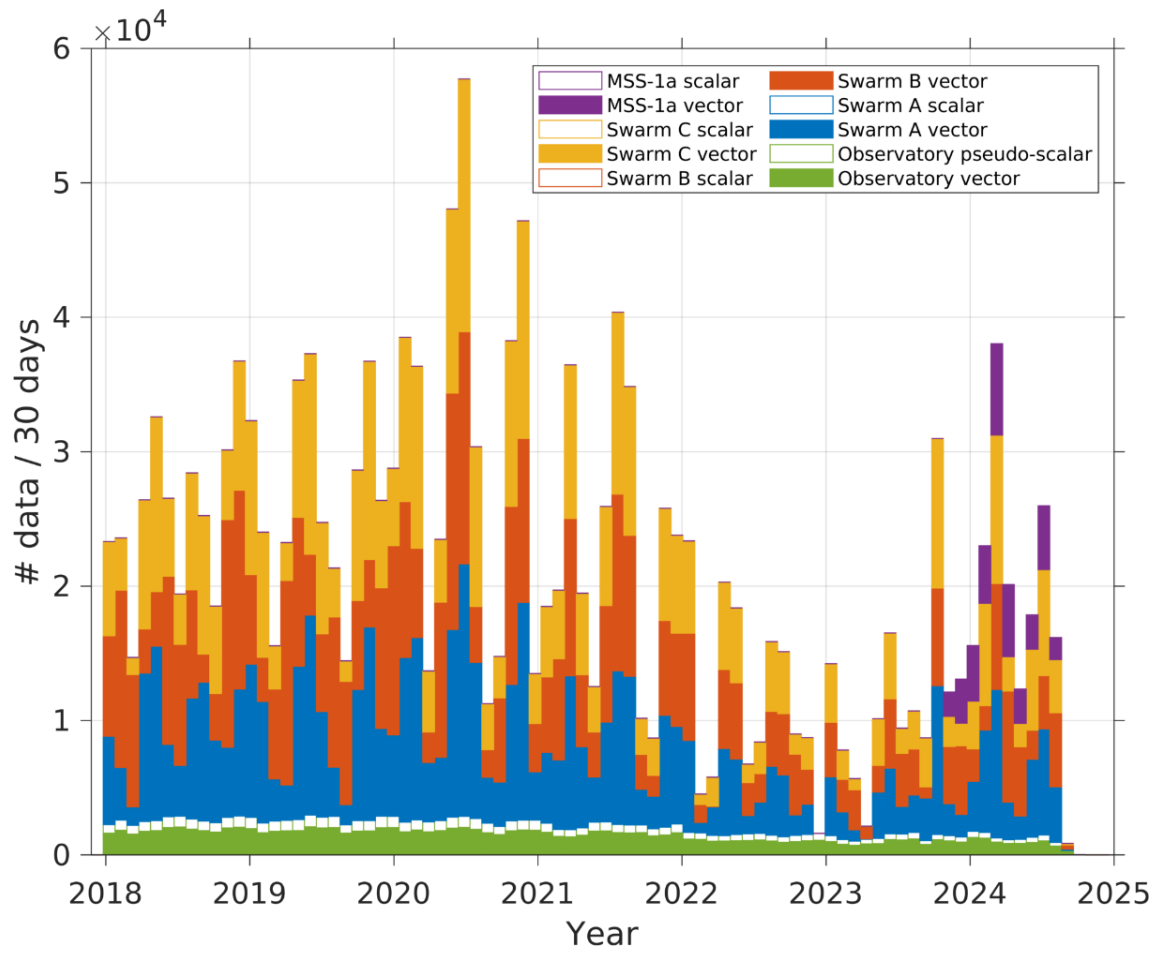


Figure 1: (Top) Stacked histogram of data coverage in time, binned each 30 days. Solid bars show vector data, hollow bars show scalar data. (Bottom) Distribution of data by GMD latitude and time, satellite vector and scalar data is combined.

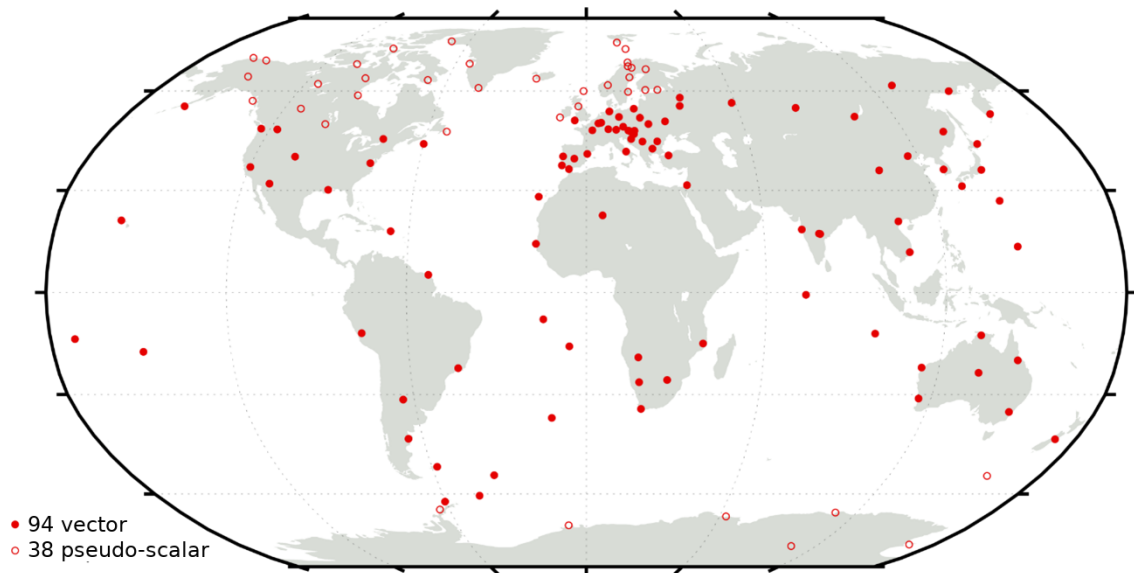


Figure 2: Map of the 132 observatory locations providing hourly data. Closed circles for the 94 locations that provide vector data, open circles for the 38 locations above GMD latitudes $|55^\circ|$ that provide projected scalar data.

2. Data weighting

2.1 Swarm and MSS

Satellite data variances were calculated from a combination of noise terms based on:

- Along-track standard deviation calculated over each 20 s segment of 1 Hz data, in each vector component, and for the scalar field (nT).
- External field activity interpolated from the three geographically nearest magnetic observatories that form a geographic triangle about the datum, as described by the LAVA index (in nT) [see Thomson *et al.*, 2010]
- Spatially uniform noise (2 nT standard deviation)
- A function of solar zenith angle, z , $(1 + \cos(z))^2$ (in nT)

These variances were then scaled by data density within 1° equal-area tesserae, such that the dense high latitude data are down weighted.

2.2 Ground observatories

Ground observatory data were given a simpler prior variance:

- Spatially uniform noise for vector data below $|55^\circ|$ GMD latitude (2 nT standard deviation)
- Spatially uniform noise for projected scalar data above $|55^\circ|$ GMD latitude (6 nT standard deviation)
- A function of solar zenith angle, z , $(1 + \cos(z))^2$ (in nT)

These variances were then scaled by data density within 5° equal-area tesserae, to account for regions, such as Europe, with very dense coverage. A final scaling factor was applied to the variances of all observatory data such that the total weight is roughly 10% that of the total weight of all satellite data.

3. MEME parent model methodology

The BGS IGRF-14 candidate models are derived from the BGS Model of Earth's Magnetic Environment (MEME) parent model. This MEME co-estimates several field sources simultaneously as described below. The methodology broadly follows that of our IGRF-13 candidate, described by Brown *et al.* [2021]. All data and model parameterisations are in the NEC coordinate frame, unless otherwise specified.

Core field:

- spherical harmonic degree and order 15
- order 6 B-spline time dependence
- 6 month spaced knots from 2018.0 to 2025.0

- regularised time integral of the 3rd time derivative of the radial magnetic field over the core-mantle boundary, and 2nd time derivative of the radial magnetic field over the core-mantle boundary at the end knots
- 4845 parameters

Crustal field update (a prior BGS crustal field model for degrees 16 to 100 is removed from all input data):

- static in time, described from degrees 16 to 30
- 705 parameters

Large-scale slowly varying external field:

- spherical harmonic degree and order 1
- order 2 B-spline time dependence
- 3 month spaced knots from 2018.0 to 2025.0
- 87 parameters

Large-scale rapidly varying external and induced field:

- spherical harmonic degree and order 1
- constant within each 3-month knot defined above
- scaled by the external and induced degree and order 1 coefficients of the VMD index [Thomson & Lesur, 2007] until 2024/06/30, and by the Dst index for the most recent data when VMD cannot robustly be determined due to insufficient spatial distribution of available data
- 174 parameters

Periodic variations:

- external and induced
- constant in time
- spherical harmonic degree and order 1
- sine and cosine terms for annual and semi-annual variations
- 24 parameters
- external
- constant within annual knots from 2018.0 to 2025.0
- spherical degree 1, order 1 (non-zonal)
- offset, sine and cosine terms for annual variations parameterised in sun-synchronous longitude
- 48 parameters

Observatory crustal bias updates (a prior crustal field model for degrees 16 to 100 is removed from all input data):

- static offsets for each vector component, or the scalar at high latitudes, at each observatory location to account for unresolved local crustal fields captured in the full field data
- 528 parameters

The model inversion solves for 6,411 parameters from 5,162,040 data by iteratively reweighted least squares, using a null starting model and an L2 norm with Huber reweighting of residuals. Regularisation is applied only to the time varying core field and is governed by three damping parameters that control the damping at each model end knot, and the time integral, respectively.

The final model fit has an overall formal unweighted standard deviation of 1.61 nT, a summary of weighted mean and root-mean-square residual misfit is given in Table 2.

Table 2: Number of data by type, and the mean and root-mean-square misfits between model and data, weighted by the inverse of the data covariances and final data Huber weights. Satellite data with subscript ‘L’ indicate low latitude data at GMD latitudes below $|55^\circ|$, values with subscript ‘H’ indicate high latitude data at GMD latitudes above $|55^\circ|$. Observatory vector and projected scalar data are only used in the regions below and above $|55^\circ|$ GMD latitude, respectively. Residuals are in NEC coordinates.

			Mean [nT]				RMS [nT]			
	# vector triples	# scalar	B _N	B _E	B _C	F	B _N	B _E	B _C	F
All Satellite	1,584,627	58	0.00	0.00	0.00	0.31	0.53	0.84	0.51	1.15
All Satellite _L	887,074	42	0.00	0.00	0.00	0.40	0.34	0.54	0.39	1.10
All Satellite _H	697,553	16	0.08	-0.01	0.00	-0.08	2.23	2.44	0.73	1.33
Obs.	119,836	48,593	0.00	0.00	0.00	0.02	1.13	1.07	0.27	6.28
Swarm A _L	275,729	7	0.00	0.00	-0.01	1.79	0.87	0.48	0.34	2.26
Swarm A _H	232,084	15	0.06	-0.02	0.00	-0.06	1.98	2.67	1.21	1.30
Swarm B _L	295,588	34	0.02	0.00	0.01	0.36	0.89	0.64	0.45	1.01
Swarm B _H	232,194	1	0.14	0.01	0.00	-6.04	2.94	2.21	0.46	6.04
Swarm C _L	278,662	0	0.00	0.00	-0.01	-	0.19	0.50	0.37	-
Swarm C _H	233,275	0	0.07	-0.04	-0.01	-	2.04	2.54	1.36	-
MSS-1a _L	37,095	1	-0.07	0.00	-0.01	-0.59	1.55	0.93	0.61	0.59

4. Parent Model Analysis

The misfit statistics in Table 2 describe a good fit of the model to the input data. Biases (residual means) are generally zero for data at low latitudes, and small for high latitude data or the limited number of satellite scalar data used. We include MSS-1a data for the first time in our parent model, and find it is compatible with Swarm data and of similarly high quality. We find higher RMS misfit for MSS-1a data in all vector components compared to low latitude Swarm data (130% for X, 170% for Y, 160% for Z), but overall the RMS values are very small. MSS-1a data at low latitudes has a smaller RMS in all components than for high latitude Swarm data.

Model fit and unmodelled residuals for example input observatory timeseries are shown at a low and high latitude observatory in Figure 3 and Figure 4, respectively. The unmodelled vector residuals can be seen to have a very low bias and typical spread $<|10\text{ nT}|$. Some apparently geophysical signal remains visible in Figure 3 – residuals with correlation to the rapid, large-scale magnetosphere (i.e. D_{st}) remain in the X component, and there is an annual and semi-annual periodic trend in the Y and Z components. This suggests that the external components, or related induced fields, of our parent model could be expanded to capture additional signal, though the fit overall is good. The variance of residuals is seen to increase during periods of high geomagnetic activity, despite the strict data selection applied (e.g. during the Kp=9 storm in May 2024). It is possible that we could perform a stricter data selection, or that additional freedom for the magnetospheric components of our external field model to vary in time, either through model parameterisation or expansion of the VMD index parameterisation, could improve the model fit further. In Figure 4 showing high latitude scalar field residuals, while the residual spread is greater (typically $<|100\text{ nT}|$), it is less clear that large scale geophysical signals remain unmodelled, as the residuals are dominated by the small spatial scale and short timescale variations of external sources in the auroral and polar regions.

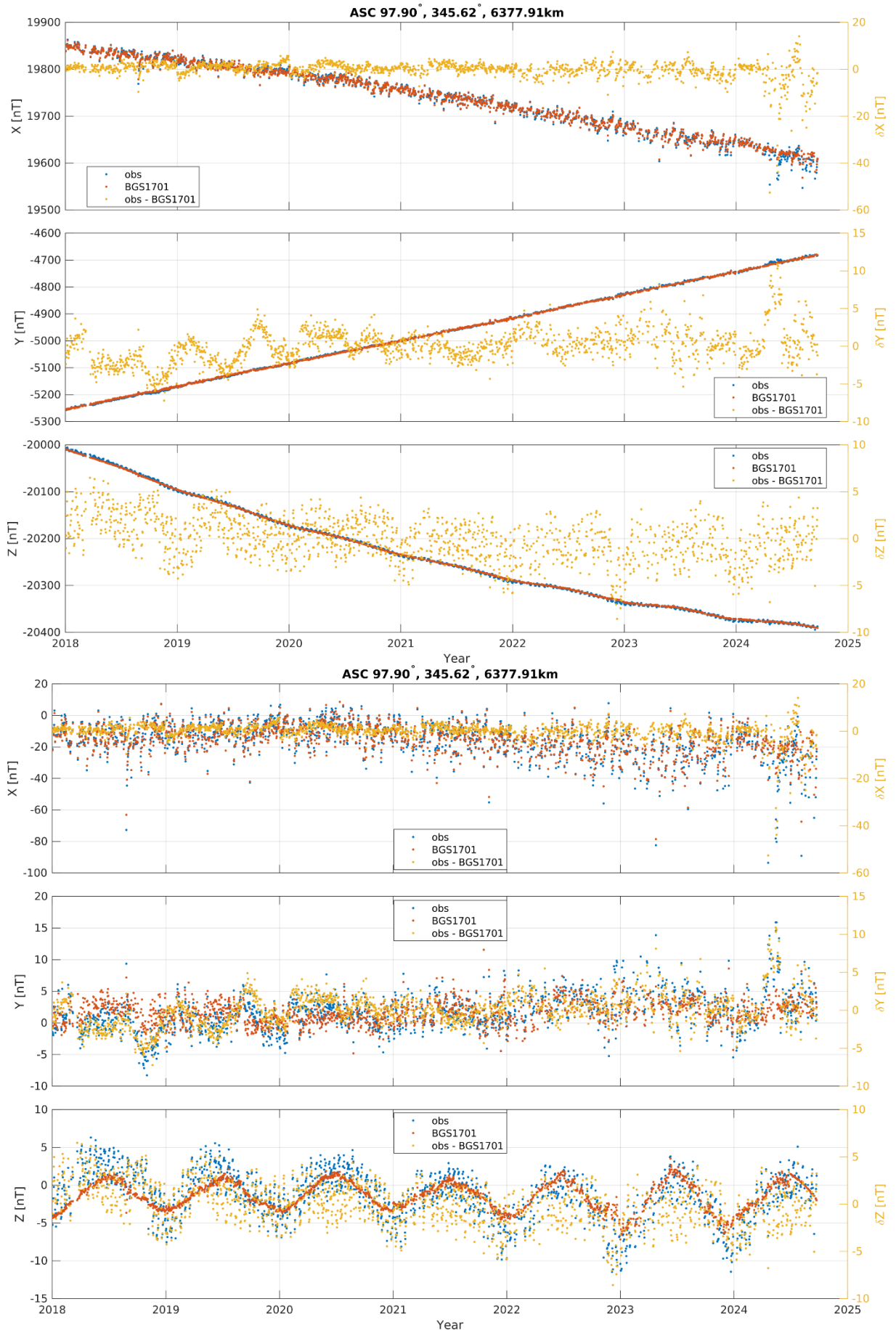


Figure 3: (Top) Input observatory hourly mean data, parent model, and unmodelled residuals in the X, Y, Z components at Ascension Island observatory, South Atlantic. (Bottom) As top panels, but having subtracted the modelled core, crust and observatory bias components from both input data and total model, and recalculated the unmodelled residuals. Residuals are plotted on right axes in all panels.

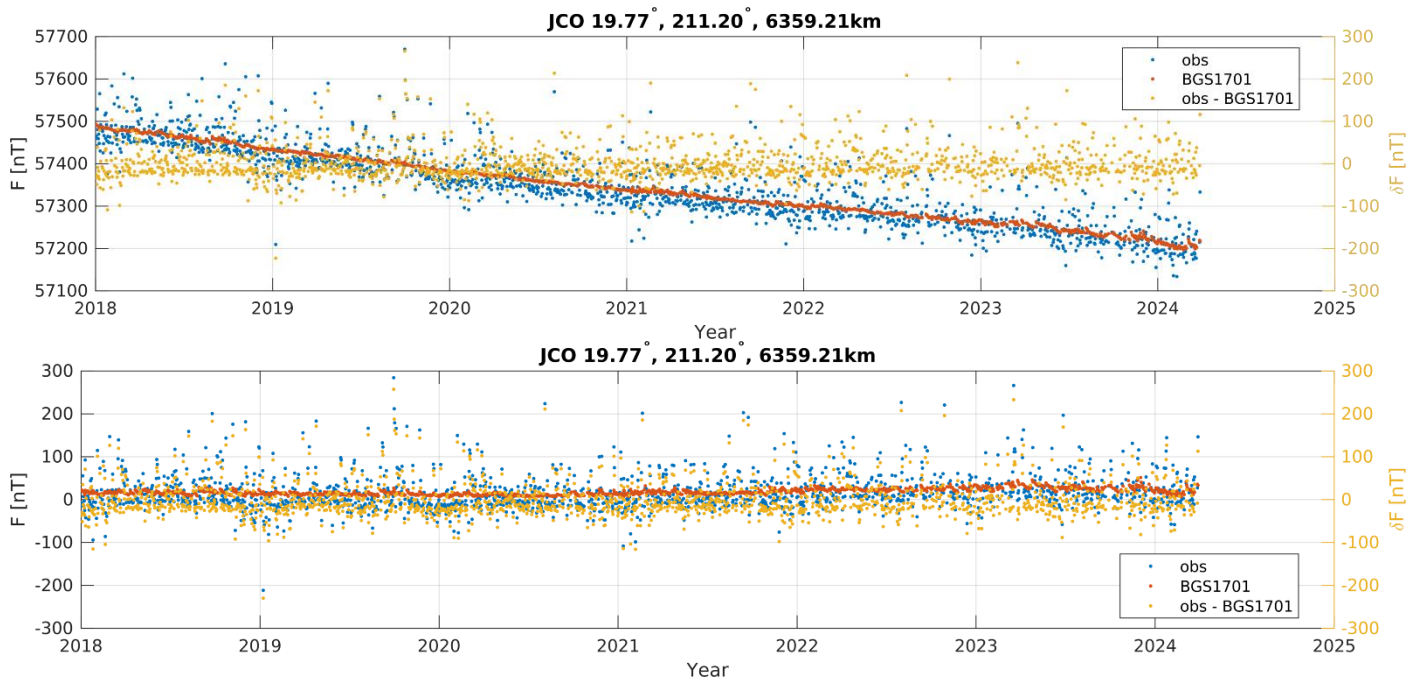


Figure 4: As Figure 3, (Top) Total model, (Bottom) External component, but for the F component at Jim Carrigan Observatory in Alaska, USA.

5. Derivation of IGRF candidate models

The three BGS candidate models were derived from MEME in the following manner. No formal uncertainties are provided with any of our candidate models.

5.1 DGRF main field at 2020.0

The main field at 2020.0 was taken directly from the core spline component of MEME, truncating to degree 13.

5.2 IGRF main field at 2025.0

The main field at 2025.0 was extrapolated from the core component of MEME, then truncated to degree 13. The main field of the MEME core component at 2024.0 was used as a datum, to which we added the mean annual core secular variation for the period 2023.25 to 2024.25, sampled at eleven equally spaced time increments, inclusive of the end times, from the spline first derivative.

5.3 Secular variation for 2025.0—2030.0

We use the steady core flow and acceleration formalism as given in Whaler & Beggan [2015] to estimate the ‘average’ flow and acceleration over 2021.0 to 2024.0. We then forward propagate the estimated main field coefficients of the BGS IGRF2020 candidate from 2025.0 to 2030.0. We compute the difference between 2030.0 and 2025.0 and divide by five to produce the mean annual SV coefficients for our candidate model (up to degree and order 13) which is then truncated to degree 8 as required.

In detail, we use the monthly SV and SA magnetic field values of the MEME parent model output from 2021.0 to 2024.0 to compute the steady core flow and steady core acceleration over this 3-year period. The core flows were computed using an L1-norm iterative-reweighting scheme to fit the flow and acceleration to the SV and SA coefficients (up to degree and order 14 and 8, respectively). We apply also a tangentially geostrophic constraint to the L1-norm solution (see Beggan & Whaler [2008]) before solving for the steady flow and acceleration. Both toroidal and poloidal flow and acceleration are solved for simultaneously. The outputs consist of a steady flow model and steady acceleration model for the period covering 2021.0 to 2024.0.

The forecast from 2025.0 to 2030.0 was made using monthly time-steps (one-twelfth of a year). At each time-step, the Gaunt and Elsasser matrices are computed using the main field model and secular variation from the preceding month. The SV and SA are computed from the Gaunt-Elsasser matrix multiplied by the steady flow and acceleration model and added to the main field to step forward by a month.

The process is repeated from 2025.0 to 2030.0. The main field coefficients for 2025.0 are subtracted from main field coefficients of 2030.0 to compute the field change over five years. The annual SV is computed by dividing the difference by 5.

6. References

- Beggan, C., K. Whaler (2008), Core flow modelling assumptions, *Physics of the Earth and Planetary Interiors*, 167, 217-222, doi: 10.1016/j.pepi.2008.04.011.
- Brown, W. J., Beggan, C. D., Cox, G. A., & Macmillan, S. (2021). The BGS candidate models for IGRF-13 with a retrospective analysis of IGRF-12 secular variation forecasts. *Earth, Planets and Space*, 73, 1-21, doi: 10.1186/s40623-020-01301-3.
- Olsen, N., H. Lühr C. C. Finlay, T. J. Sabaka, I. Michaelis, J. Rauberg and L. Tøffner-Clausen (2014), The CHAOS-4 geomagnetic field model. *Geophysical Journal International*, 197(2), 815-827, doi: 10.1093/gji/ggu033.
- Thomson, A. W. P., B. Hamilton, S. Macmillan and S. J. Reay (2010), A novel weighting method for satellite magnetic data and a new global magnetic field model, *Geophysical Journal International*, 181, 250-260, doi: 10.1111/j.1365-246X.2010.04510.x.
- Thomson, A. W. P. and V. Lesur (2007), An Improved Geomagnetic Data Selection Algorithm for Global Geomagnetic Field Modelling. *Geophysical Journal International*, 169, 951-963 doi: 10.1111/j.1365-246X.2007.03354.x.
- Whaler, K. A., and C. D. Beggan (2015), Derivation and use of core surface flows for forecasting secular variation. *Journal of Geophysical Research: Solid Earth*, 120, 1400-1414, doi: 10.1002/2014JB011697.